Geochemistry Geophysics Geosystems G3

Article
Volume 14, Number 1
31 January 2013
doi:10.1029/2012GC004451
ISSN: 1525-2027

Published by AGU and the Geochemical Society

Seismic anisotropy around subduction zones: Insights from three-dimensional modeling of upper mantle deformation and SKS splitting calculations

M. Faccenda
Dipartimento di Geoscienze, Università di Padova, Padova, Italy

School of Geosciences, Monash University, Clayton, Victoria, Australia (manuele.faccenda@gmail.com)

F. A. Capitanio
School of Geosciences, Monash University, Clayton, Victoria, Australia

[1] Inferring the circulation of the mantle around subducting plates from surface measurements of shear wave splitting patterns remains to date elusive. To assist the interpretation of the seismic signal and its relation with the mantle circulation pattern, we present a new methodology to compute the seismic anisotropy directly from the flow in the upper mantle of 3-D numerical models of Earth-like subduction. This computational strategy accounts for the non-steady-state evolution of subduction zones yielding mantle fabrics that are more consistent with the deformation history than previously considered. In the subduction models, a strong mantle fabric develops throughout the upper mantle with a magnitude of the anisotropy that is proportional to the amount of subduction and is independent of the subduction rate. The sub-slab upper mantle is characterized by two domains with different fabrics: at shallow depth, the mantle entrained with the subducting slab develops trench-perpendicular directed anisotropy due to simple shear deformation, while in the deeper mantle, slab rollback induces pure shear deformation causing trench-parallel extension and fast seismic directions. Subducting plate advance favors the development of the fabric in the entrained mantle domain, while slab retreat increases the trench-parallel anisotropy in the deeper upper mantle. In the deeper domain, the strength of the fabric is proportional to the horizontal divergence of the flow and weakens from the slab edges toward the center. As such, strong trench-parallel anisotropy forms below retreating and relatively narrow slabs or at the margins of wider plates. The synthetic SKS splitting patterns calculated in the fore arc are controlled by the magnitude of the anisotropy in the upper domain, with trench-perpendicular fast azimuths in the center of large plates and trench parallel toward the plate edges. Instead, above relatively narrow, retreating slabs (≤600 km and low subduction partitioning ratio [SPR]), azimuths are trench parallel due to the strong anisotropy in the lower sub-slab domain. In all models, the anisotropy in the back arc and on the sides of the subducting plate is, respectively, trench perpendicular and sub-parallel to the return flow at depth. Results from our regional scale models may help to infer the flow and composition of the upper mantle by comparison with the wide range of subduction zones seismic data observed globally.

Components: 13,500 words, 10 figures, 1 table.

Keywords: seismic anisotropy; subduction zone; strain-induce LPO; SKS splitting; numerical modeling.

Index Terms: 0545 Computational Geophysics: Modeling (1952, 4255, 4316); 3902 Mineral Physics: Creep and deformation; 7240 Seismology: Subduction Zones (1207, 1219, 1240).

Received 20 September 2012; **Revised** 20 December 2012; **Accepted** 20 December 2012; **Published** 31 January 2013.

Faccenda, M., and F. A. Capitanio (2013), Seismic anisotropy around subduction zones: Insights from three-dimensional modeling of upper mantle deformation and SKS splitting calculations, *Geochem. Geophys. Geosyst.*, *14*, 243–262, doi:10.1029/2012GC004451.

1. Introduction

[2] Plate tectonics is the surface expression of the convecting Earth's mantle. There is geophysical evidence that the horizontal and vertical motions of rigid tectonic plates are strongly coupled with the flow in the underlying, viscous upper mantle [*Richardson et al*., 1979; *Montagner and Tanimoto*, 1991]. Therefore, by reconstructing the motions of the lithosphere in time, it is possible to infer the upper mantle flow patterns. Conversely, by inferring upper mantle flow patterns, it is possible to indirectly reconstruct the recent kinematic and dynamic history of the lithosphere.

[3] Seismic anisotropy generated by strain-induced lattice/crystal preferred orientation (LPO/CPO) of intrinsically anisotropic minerals is commonly used to infer mantle flow and its relations with plate motions [*Park and Levin*, 2002]. Upon traveling through an anisotropic medium, a shear body wave is split in two orthogonally polarized components, with the fastest being polarized in the plane with the highest shear wave velocity. Shear wave splitting (SWS) is defined by two parameters: the time delay δt between the arrival of the fast and slow wave components and the azimuth ϕ of the fast wave component. While the first depends on the intrinsic anisotropy and spatial extent of the anisotropic region along the ray path, the second provides information about the geometry of the anisotropic fabric.

[4] At subduction zones, the splitting of several phases (local S, source-side S, and vertically traveling SKS waves) is measured in order to discriminate among different anisotropy sources like those potentially located in the supra-slab, slab, and sub-slab mantles [*Long and Silver*, 2009; *Foley and Long*, 2011; *Di Leo et al*., 2012]. A strong trench-parallel anisotropy is commonly found in the sub-wedge mantle (i.e., slab + sub-slab mantle), with δt possibly proportional to the trench migration rate [*Long and Silver*, 2009]. Although less systematic, the anisotropy in the mantle wedge is generally oriented parallel to the trench in the fore arc and progressively rotates at high angles to the trench in the back arc [*Kneller et al*., 2005]. SKS splitting patterns are characterized by trench-parallel fast azimuths in 90% of the fore arcs and trench perpendicular in the back arc, while at the edges of the subduction zone, fast azimuths align in a circular pattern (e.g., [*Baccheschi et al*., 2007; *Zandt and Humphreys*, 2008; *Russo and Silver*, 1994; *Long and Silver*, 2009]) (Figure 1).

[5] The interpretation of SWS splitting patterns in terms of the mantle flow is not always warranted and is, in fact, complicated by several mechanisms. Indeed, although LPO/CPO is produced extensively in the viscous upper mantle where deformation is accommodated mostly by dislocation creep [*Nicolas and Christensen*, 1987; *Kawazoe et al*., 2009], laboratory experiments and analytic solutions indicate that the orientation of the seismic fast direction of olivine (the upper mantle most abundant mineral) varies as a function of the type of deformation and pressure, temperature, water content, and deviatoric stress conditions [*Nicolas et al*., 1973; *Zhang and Karato*, 1995; *Kaminski and Ribe*, 2002; *Karato et al*., 2008] (see Supporting Information[1]). Furthermore, preferred orientation of structures like faults, gas- or fluid-filled cracks, tabular intrusions, and fine layering of two or more media with different elastic properties can produce an additional anisotropic source (shape preferred orientation; SPO), provided the spacing is much smaller than the seismic wavelength [*Backus*, 1962; *Crampin*, 1994]. At subduction zones, an additional complication is represented by hydrous and highly anisotropic phases like serpentine, talc, and chlorite that are likely to be present in the cold nose of the mantle wedge and in the upper part of the subducting slab [*Faccenda et al*., 2008; *Katayama et al*., 2009; *Mookherjee and Capitani*, 2011].

[6] A promising approach towards a rigorous interpretation of SWS measurements is to compare them with the predictions of numerical and experimental flow models and thus narrow the range of plausible models that can explain a given dataset [*Long et al*., 2007]. Pioneering studies by *Hall et al*. [2000] and *Long et al*. [2007] have combined flow fields computed numerically with anisotropy versus Finite Strain Ellipsoid (FSE) relationships to calculate the elastic coefficients of a layered medium beneath a subduction zone that was subsequently probed by synthetic SWS measurements. These studies focused on the mantle wedge with 2D kinematic models of subduction where the geometry and velocity of a

[1] All Supporting Information may be found in the online version of this article.

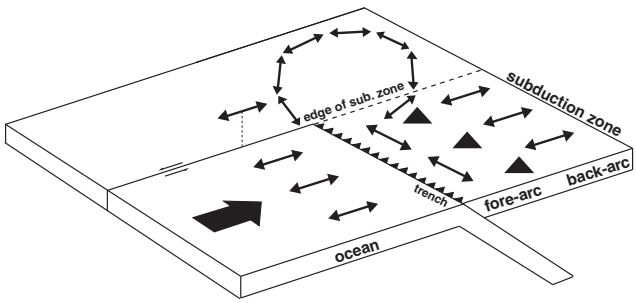

Figure 1. Geodynamic sketch showing the commonly observed SKS splitting patterns at subduction zones. The orientations of the fast azimuths in the fore arc are not indicative of the full range of observations. The transform margin on the side of the subducting plate is chosen arbitrarily. The black triangles are for the volcanic arc.

steady-state flow were prescribed. However, anisotropy versus FSE relationships underestimate the magnitude of the calculated anisotropy for large strains because dynamic recrystallization is neglected [*Ribe*, 1992]. More recently, instantaneous mantle flow solutions have been coupled with more realistic models of LPO development based on dynamic recrystallization and plastic deformation to study the upper mantle strain-induced anisotropy [*Becker et al*., 2006; *Becker et al*., 2008; *Lassak et al*., 2006; *Miller and Becker*, 2012]. All these previous studies considered a steady-state upper mantle flow. Although this assumption has been proved correct in intra-oceanic settings, where the flow has been rather constant over the last 43 Ma [*Becker et al*., 2003], it might not be valid in proximity of, for example, migrating subduction zone trenches, or mid-ocean ridges which are frequently observed on Earth [*Heuret and Lallemand*, 2005; *Masalu*, 2007].

[7] In this paper, we quantify the seismic anisotropy due to crystal LPO in 3-D numerical subduction models and estimate synthetic SKS splitting with a methodology recently introduced by *Faccenda and Capitanio* [2012]. Our models use the full mantle flow developing during the subduction of an oceanic plate to compute the strain-induced, history-dependent LPO fabric, taking into account dynamic recrystallization and other creep mechanisms. We address here the role of the plate width during subduction and investigate the relation between mantle flow and the synthetic seismic anisotropy that can be measured at the surface. We then discuss the implication for the data observed around subduction zones on Earth.

2. Methodology

[8] In this section, we present our workflow based on three open source software codes that have been modified for inter-compatibility, computational speed, 3D Cartesian geometry, and, more importantly, to account for a physically consistent, time-dependent development of strain-induced anisotropy. A fourth open source software code (MTEX, http://code.google.com/p/mtex/) [*Mainprice et al*., 2011] has been used to plot pole figures of crystal aggregate olivine LPOs and elastic tensors.

2.1. Mechanical Flow Modeling

[9] We carried out 3D mechanical simulations of oceanic plate subduction with Underworld, a geodynamic framework based on a Lagrangian Particle-In-Cell Finite Element scheme (http://www.underworldproject.org/index.html) [*Moresi et al*., 2007]. Under the incompressibility assumption, the equations for the conservation of mass and momentum are (see Table 1 for symbols explanation)

$$\nabla \cdot \vec{v} = 0 \tag{1}$$

$$\nabla \tau - \nabla P = -\vec{g}(\rho_0 + \Delta\rho) \tag{2}$$

[10] Subduction is modeled as the sinking in the viscous mantle of a stiffer oceanic-like plate, under

Table 1. Model Parameters, Symbols, and Geometry

Parameter	Symbol	Value	Dimension
Velocity vector	$\vec{v}$		$m\,s^{-1}$
Deviatoric stress tensor	τ		Pa
Total pressure	P		Pa
Lithostatic pressure	P_L		
Acceleration of gravity vector	$\vec{g}$	$g_x = 0$; $g_y = 9.81$; $g_z = 0$	$m\,s^{-2}$
Reference density	ρ_0	3300	$kg\,m^{-3}$
Density contrast	$\Delta\rho$	40, 57, 80	$kg\,m^{-3}$
Slab top layer			
Cohesion	C	20	MPa
Coefficient of friction	μ	0.01	
Viscosity	η	10^{24}	Pa s
Thickness	h	30	km
Slab core			
Viscosity	η	10^{24}	Pa s
Thickness	h	30	km
Slab basal layer			
Viscosity	η	3×10^{21}	Pa s
Thickness	h	20	km
Upper mantle			
Second invariant of the strain rate tensor	$\dot{\varepsilon}_{II}$		s^{-1}
Power-law exponent	n	3.5	
Newtonian viscosity	η_0	10^{19}	Pa s
Effective viscosity	η_{eff}		Pa s
Thickness	h	660	km
Lower mantle			
Viscosity	η	10^{23}	Pa s
Thickness	h	340	km

the pull of its own negative buoyancy. The dimensions of the model's domain are $(x,y,z) = 4000 \times 1000 \times 4000$ km with $96 \times 64 \times 96$ elements, where y is depth with a symmetry plane in $z = 0$ (Figure 1). The initial conditions is that of a 2200 km long oceanic plate of a constant density contrast with the mantle (Table 1), with a 200 km long slab dipping 60° attached to its margin. Then subduction becomes self-sustaining under the increasing pull of the slab, as it extends to the bottom of the upper mantle (Figure 2). Free slip boundary conditions are applied to the top and side boundaries perpendicular to the z direction, while no slip is imposed on the bottom boundary. The computational domain is periodic along the x direction. As in our models, no volcanic arc forms; for the sake of the results discussion, we assume that the fore-arc/back-arc transition at the surface is the projection of the 100 km isobath, a value that represent the global average depth to the top of the slab beneath volcanic arcs [*Syracuse and Abers*, 2006]

[11] The oceanic plate viscosity distribution is simplified to a strong viscous top (10^{24} Pa s, 60 km thick) and a weaker lower layer (3×10^{22} Pa s, 20 km thick) [*Capitanio et al.*, 2009]. Weakening in the highly viscous top 30 km is achieved with a depth-dependent von Misses yielding criterion $\tau_Y = C_0 + \mu P_L$ [*Moresi and Solomatov*, 1998], with cohesion $C_0 = 20$ MPa and friction $\mu = 0.01$. This simple layered rheology captures the essential characteristic of the lithosphere's yielding profile where the strength in the top (partially brittle) and basal (low viscosity) layers is lower than that in the plate's interior under stress conditions typical of trench zones [e.g., *Kohlstedt et al.*, 1995]. Furthermore, the visco-plastic top layer ensures bending of the slab at the trench and lubrication at the plates contact while preventing the whole oceanic plate from sinking into the asthenospheric mantle.

[12] Although the upper mantle and transition zone rocks have different physical parameters, for simplicity we assume that the upper, 660 km thick layer is homogeneous. Here, deformation is accommodated by dislocation creep according to the mechanical flow law:

$$\eta_{\text{eff}} = \eta_0 \left(\frac{\dot{\varepsilon}_{II}}{\dot{\varepsilon}_{II0}} \right)^{\frac{1-n}{n}} \tag{3}$$

where η_{eff} is the effective, non-Newtonian viscosity, η_0 is the viscosity at the reference second invariant of the strain rate tensor $\dot{\varepsilon}_{II0}$, and $n = 3.5$ is the power-law exponent derived empirically from laboratory experiments on olivine aggregates [*Karato and Wu*, 1993; *Hirth and Kohlstedt*, 2003]. The lower 340 km of the model domain has a constant viscosity of 10^{23} Pa s that simulates a more viscous lower mantle, resisting subduction.

[13] Our simplified rheological model for viscous flow does not take into account for the temperature, pressure, and water content dependence of the viscosity, and for the olivine to β-spinel phase transition occurring at the 410 km discontinuity [e.g., *Karato et al.*, 2001]. Moreover, while we assume that viscous flow is solely by dislocation creep, deformation in the upper mantle can be accommodated by intra-granular diffusion and Grain-Boundary Sliding (GBS, driven either by diffusion or dislocation creep along grain

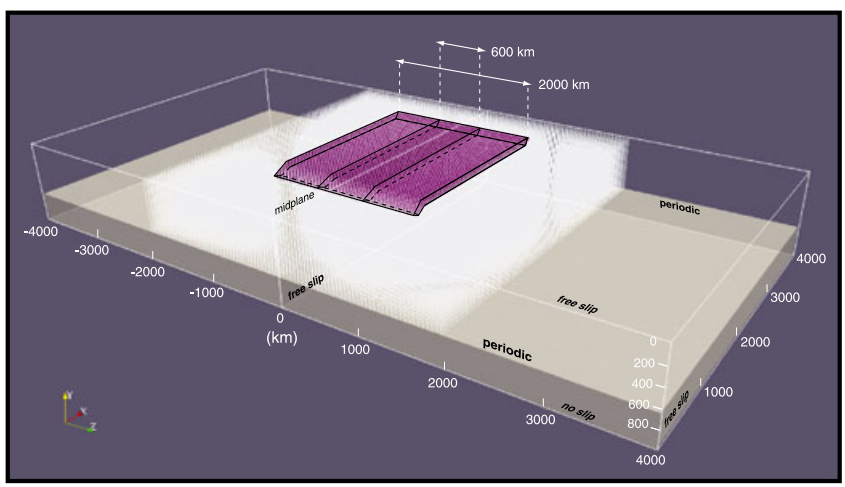

Figure 2. Initial numerical setup. The light gray region at the bottom is the lower mantle. Purple surfaces are density contours of oceanic plates 600 (Model A) and 2000 (Model B-C) km wide. The white dots indicate the initial position of crystal aggregates. The vertical plane at $z = 0$ km (midplane) is the symmetry plane.

boundaries) [*Hirth and Kohlstedt*, 2003]. As diffusion creep processes tend to produce no LPO, our strain-induced mantle fabrics have to be considered as upper bound estimates. Nevertheless, despite a more complex rheological model would better reproduce mantle flow, we believe that the non-Newtonian viscous flow law used here gives a good first order approximation of the creep in the upper 660 km of the mantle, especially nearby sliding plates where the stress/strain rate are high, and dislocation creep is the preferred deformation mechanism forming seismic anisotropy.

[14] For simplicity, we show results from two end members, that is slab models of half width 300 km (narrow plate, Model A) and 1000 km (large plate, Model B-C).

2.2. Estimation of the Strain-induced LPO in the Upper Mantle

[15] The lattice preferred orientation (LPO) of rocks at upper mantle conditions develops during deformation with a number of mechanisms that span from plastic deformation to dynamic recrystallization (by sub-grain rotation and grain-boundary migration) and grain-boundary sliding [*Kaminski et al*., 2004]. The difficulty in reproducing such a complex behavior has led to the generation of alternative and simpler models for the estimation of the LPO and associated seismic anisotropy.

[16] The orientation of the olivine seismically fast axis is usually estimated under the assumption that the mantle flow is in steady state. This flow is described by means of the ISA and the Grain Orientation Lag parameter Π [*Kaminski and Ribe*, 2002]. If $\Pi << 1$, the ISA orientation is constant in space, and therefore, the LPO will quickly align with the ISA. Conversely, when $\Pi >> 1$, crystal rotation is unable to keep up with the rapid changes of the ISA due to dynamic recrystallization, and LPO will depend on the complex deformation history. It has been shown that this method does not give a complete coverage of the anisotropy in the area under study because Π is quite large in most convective regions [*Becker et al*., 2006; *Conrad et al*., 2007; *Jadamec and Billen*, 2010], and moreover, it does not provide a measure of the strength of the anisotropy. We have computed the orientation of the ISA and Π in our models, and consistently with previous studies, we found that $\Pi >> 1$ in most of the model domain and therefore we drop it in favor of more accurate calculations.

[17] Another way to estimate the LPO and the associated anisotropy is calculating the FSE and considering the orientation and length of the longest axis of the FSE as the olivine fast *a* axis [*McKenzie*, 1979; *Hall et al*., 2000; *Long et al*., 2007; *Kneller and van Keken*, 2008]. However, this method is limited to regions with small variations of the velocity gradients ($\Pi << 1$) because, as previously discussed, dynamic recrystallization delays the alignment of the olivine *a* axis with the maximum stretch direction.

[18] The development of crystal aggregates LPO can be estimated with more sophisticated codes that account for the basic macrophysics of the deformation mechanisms [*Wenk and Tomé*, 1999; *Kaminski et al*., 2004]. One such code is D-Rex (http://www.ipgp.fr/~kaminski/) [*Kaminski et al*., 2004]; it calculates the development of the lattice preferred orientation (LPO) of olivine-enstatite aggregates in convective flow by plastic deformation, dynamic recrystallization (by sub-grain rotation and grain-boundary migration), and grain-boundary sliding of small grains. It is worth noting that the incorporation of enstatite results in a net decrease of the total anisotropy because its slow axis orients parallel to the olivine fast axis [*Ribe*, 1992; *Blackman et al*., 2002; *Kaminski et al*., 2004]. D-Rex has been extensively used to study the upper mantle strain-induced anisotropy at global scales [*Becker et al*., 2006; *Becker et al*., 2008] and at smaller scales, in subduction zones[*Lassak et al*., 2006; *Miller and Becker*, 2012]. D-Rex output includes the 36 components of the stiffness matrix of each crystal aggregate and its best transverse isotropy approximation calculated using the projection method of [*Browaeys and Chevrot*, 2004]. The elastic tensors can be used to calculate the seismic velocity along any given direction. The magnitude of the symmetry axis is proportional to the amount of transverse isotropy and, together with its orientation, gives a quick estimate of the geometry of the elastic anisotropy. As transverse isotropy is not properly approximated at low finite strains (i.e., weak LPO), we will show the orientation and magnitude of the symmetry axis only for aggregates with logarithmic ratio $f = \log(e_{max}/e_{min}) > 0.5$, where e_{max} and e_{min} are the largest and smallest axes of the finite strain ellipsoid (FSE).

[19] In D-Rex, the LPO of the aggregates with an initially random distribution of crystals is calculated in a 2D coordinate system. The velocity gradients are interpolated along the aggregate trajectories traced backward in time on a single velocity field. This implies that the system is at steady-state flow conditions for long enough for any previous fabric can be overprinted. However, this is not the case for subduction zones where the velocity gradient fields vary in time. More in general, convective

mantle flows are non-uniform and non-steady-state, and a different approach to the modeling of the LPO and of the seismic anisotropy is needed.

[20] In order to calculate the evolution of the upper mantle fabric from early subduction through the whole model run, D-Rex has been modified to account for forward advection of aggregates and 3-D flow. A mesh of Lagrangian particles regularly spaced in the horizontal (30/50 km for narrow/large plates, respectively) and vertical (20 km) directions is initially placed in the upper, non-Newtonian layer (0–660 km, Figure 2). Particles are advected with fourth-order Runge-Kutta scheme, and their LPOs are calculated at each time step by using a different input velocity field. This new methodology accounts for the non-steady-state evolution of geodynamic systems and, consequently, for a more physically consistent development of the LPO.

[21] Each particle is an aggregate of 1000 randomly oriented crystals with 70% A-type olivine and 30% enstatite that are representative of the upper mantle (0–410 km) composition. Aggregates at transition zone depths are assumed to be isotropic. *Mainprice* [1990] showed that β-spinel may inherit part of the olivine LPO after phase transformation at the 410 km discontinuity. For simplicity, however, the LPO and FSE of aggregates that descend below 410 km depth are reset by newly assigning a random distribution of the minerals and by setting the deformational gradient tensor

$$F_{ij} = \delta_{ij} \tag{4}$$

where δ_{ij} is the Kronecker delta function. We use the same input crystallographic parameters as in *Kaminski et al.* [2004], where the dimensionless parameters $\lambda^* = 5$, $M^* = 125$, and $\chi = 0.3$ are the nucleation rate, the "intrinsic" grain-boundary mobility and threshold volume fraction below which grain-boundary sliding takes place.

[22] Because of the large number of aggregates and computational time steps, D-Rex has been parallelized with OpenMP® that offers a complete scalability for most of the code subroutines.

[23] Figure 4 compares the upper mantle fabric resulting from subduction of a 600 km wide homogeneous plate (Model A) computed with the old and new methodologies, that is, the steady-state assumptions and the history-dependent anisotropy. The symmetry axes of the transverse isotropy projected for each crystal aggregate represent the fast seismic direction because they are nearly coincident with the maximum stretching direction of the FSE (compare Figures 3, S1, and S2). With the original D-Rex methodology, each crystal aggregate is characterized by a strong LPO because its trajectory is calculated backward in time until the imposed maximum strain ($\varepsilon = 10$) is achieved. This implies that the whole upper mantle experienced high deformation during subduction resulting

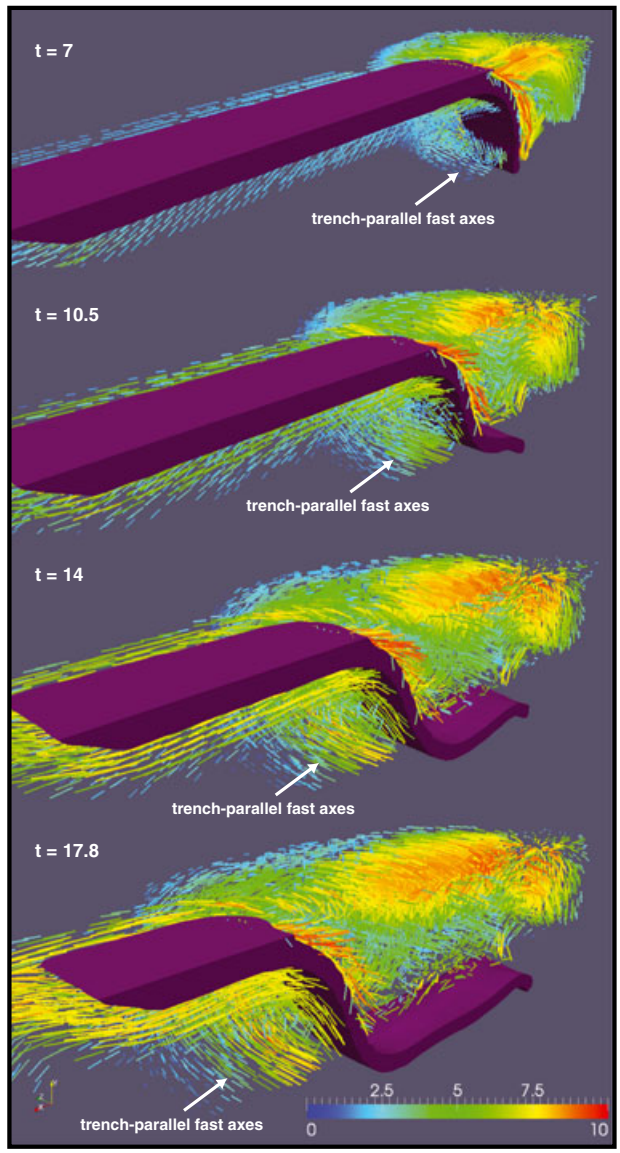

Figure 3. Snapshots of the evolution of Model A and computed mantle fabric. The purple surface is the contour of the density field around the plate. The length and color of each bar are proportional to the amount of anisotropy. Time is in Ma. During the model run, the plate sinks through the mantle and lies over the 660 km discontinuity between the upper and lower mantles. The anisotropy in the sub-slab region increases with subduction and is characterized by two domains, the shallower with trench-perpendicular fast axes and the deeper with trench-parallel anisotropy (from *Faccenda and Capitanio* [2012]).

in a widespread strong fabric. On the other hand, by using different input velocity fields and with forward advection of the crystal aggregates, the LPOs are strong closer to the subduction zone where deformation is high and vanishes away from it. Furthermore, dip-parallel fast axis at the slab boundaries and trench-parallel sub-slab anisotropy due to the rollback of the plate are more consistent with the dynamics of the subduction zone. SKS splitting patterns (see next section) are quite irregular with the original D-Rex methodology, while a toroidal pattern similar to those observed at the edge of subduction zone is obtained by using the new methodology.

[24] The sensitivity of our LPO modeling assumptions was tested in models with a narrow plate similar to Model A either by using the lower temperature end-member of $M^* = 50$, by accounting for diffusion creep or by imposing an initial, strong mantle fabric (Figure S7, see Supporting Information for a more detailed discussion). In all cases, the mantle fabric and SKS splitting patterns are similar to those obtained with the reference LPO modeling assumptions, indicating that results are quite robust in the D-Rex framework.

2.3. SKS Splitting

[25] The SKS splitting is calculated at the model surface with the routines included in the FSTRACK package (http://earth.usc.edu/~becker/data.html) [*Becker et al*., 2006]. These routines compute the harmonic response of a horizontal layer stack to an incident plane wave (5° for typical SKS arrivals) over a range of frequencies (0–25 Hz) to obtain a pulse seismogram (i.e., a series of δ functions) via inverse Fourier transform using the method of *Kennett* [1983] with anisotropic extensions [*Booth and Crampin*, 1985; *Chapman and Shearer*, 1989]. Band-pass filters from 0.1 to 0.3 Hz are then applied to construct synthetic seismograms in the SKS band (3.3 to 10 s). Successively, the splitting is determined with the cross-correlation method of *Menke and Levin* [2003]. *Becker et al*. [2012] measured the splitting at a global scale with dominant SKS period of 12.5 and 15 s and found no substantial variations in the results, except for higher time delays. Similarly, small differences are produced in the SKS splitting patterns computed with dominant SKS periods of 7 s (reference) and 15 s (Figure 5d).

[26] Because the region of interest in this study is that in proximity of the subduction zone, a 2D grid of virtual seismic stations regularly spaced (30–50 km depending on the plate width) is constructed in both horizontal directions around the trench. After recovering the fourth-order elastic tensors from each aggregate's stiffness matrix, we build beneath each seismic station and down to 400 km a vertical stack of as many horizontal layers as the number of elastic tensors within a radial distance of 50 km. This is about the SKS waves Fresnel zone at 100 km depth [*Monteiller and Chevrot*, 2011]. If the vertical distance between two or more particles is less than 25 km, the elastic tensors are merged into one single matrix whose coefficients and depth are weighted from those of the original tensors according to the radial distance. In this way, we avoid the formation of too many thin layers at depths where aggregates cluster. The thickness of each layer is half the depth difference between the particles underlying and overlying the layer elastic tensor. As the fast shear wave azimuths depend on back azimuth, the SKS splitting parameters of each seismic station are obtained by averaging all the fast azimuths and delay times measured by rotating the vertical stack of elastic tensors by 2° intervals around the y axis.

[27] Although for most mantle phases it has been found that as a general trend, the anisotropy increases with increasing temperatures while high pressures tend to make the crystals more isotropic [see *Mainprice*, 2007, for a review], seismic wave propagation was calculated using single crystal elastic tensors of olivine and enstatite measured at ambient conditions that are present in D-Rex and upper mantle density of 3.353 g/cm^3. We plan to include pressure and temperature derivative of mantle phases elastic moduli and density in future thermo-mechanical simulations.

3. Results

3.1. Model A: Narrow Plate (300 km Half Width)

[28] Subduction and its induced mantle flow are driven solely by the negative buoyancy of the subducting plate. After sinking through the mantle and adjusting over the upper-lower mantle boundary, subduction occurs by slab rollback with minor plate advance until total consumption of the plate is achieved (Figure 3). Slab rollback is accommodated by return flow from the sub-slab region to the mantle wedge, while plate subduction induces poloidal flow, which is strongest above and below the slab in mantle layers entrained at depth by the subducting plate (Figure S1a). This is a standard result for a model with no upper plate and a relatively narrow subducting plate that is compatible with

both analogue and numerical models [*Funiciello et al*., 2006; *Stegman et al*., 2006].

[29] Subduction of the oceanic plate produces a strong upper mantle fabric and considerable seismic anisotropy whose magnitude and lateral extent increase with the amount of subduction (Figure 3), consistently with the laboratory experiments indicating that the strength of the LPO and the magnitude of the anisotropy are functions of the amount of deformation, i.e., the finite strain [*Ribe*, 1992; *Zhang and Karato*, 1995; *Bystricky et al*., 2000]. In general, there is a good correlation between the computed LPO and FSE, with the fastest Vp direction (indicating the mean orientation of the olivine *a* axis) forming in average an angle of 22° with the maximum extension direction (Figure S2). Simple shear deformation dominates the mantle entrained at depth by the slab resulting in a high transverse isotropy (up to 10%) with dip-parallel fast axes (Figures 3 and 4). On the other hand, the upper mantle regions above and below the entrained mantle are dominated by pure shear deformation induced by slab rollback.

[30] In the sub-slab mantle, the retreat of the slab produces a trench-normal over-pressure component that leads to trench-parallel extension (Figure S1b). As a consequence, sub-horizontal, trench-parallel anisotropy forms below the ~100 km thick entrained mantle layer with trench-perpendicular anisotropy. The trench-parallel anisotropy in the lowermost sub-slab mantle is characterized by a strongly anisotropic core with up to 9% of transverse isotropy beneath the fore arc that extends laterally over the slab edges. At these depths, the horizontal component of the mantle flow is strongly diverging from the plate midplane and is at high angles to the trench-parallel fast symmetry axes (Figure S1a).

[31] On the sides of the subduction zone, the mantle is subjected to simple shear deformation and fast axes align parallel to the return flow (2–6% transverse isotropy). As the mantle is upwelling from areas beneath and on the sides of the slab, the fast seismic directions are generally plunging away from the mantle wedge near the plate edge.

[32] The supra-slab upper mantle is characterized by trench-perpendicular fast axes (4–8% transverse isotropy) that are due to both simple shear deformation associated with the poloidal and return flow, and pure shear deformation inducing trench-normal extension. The fast seismic directions are sub-horizontal at depths <200 km, and with increasing depth, they tend to progressively plunge downwards following the downwelling return flow. Above the subducted tip of the slab, strong anisotropy with mostly trench perpendicular and variably plunging symmetry axis develops as result of the strong velocity gradient

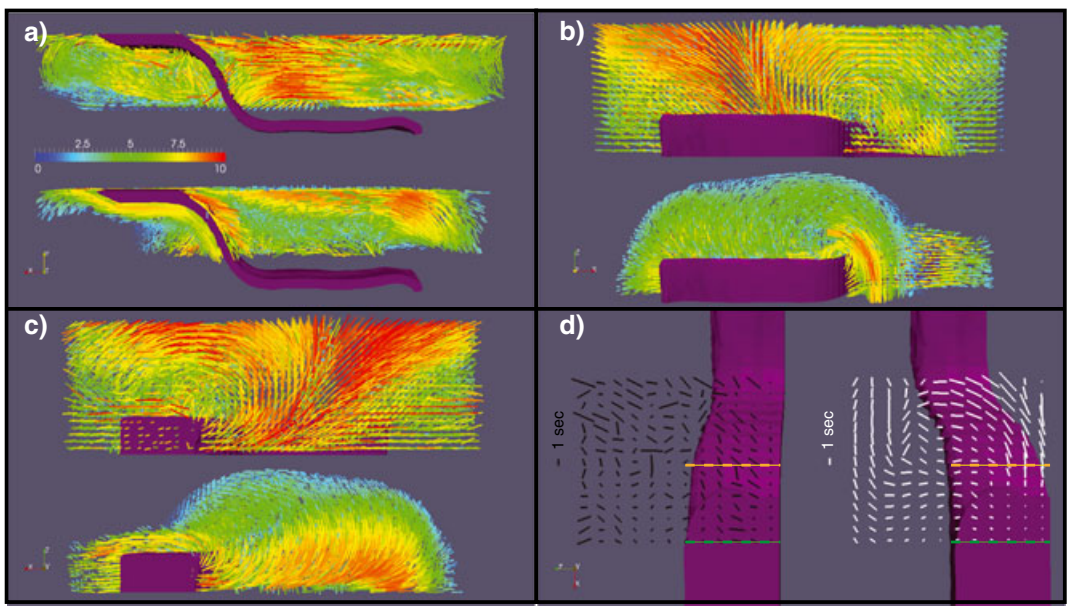

Figure 4. Comparison of the seismic anisotropy computed with the steady-state (top) and history-dependent (bottom) versions of D-Rex for Model A at $t = 17.8$ Ma (see Fig. 3). Only half of the model is shown. Plane view from the (a) midplane, (b) bottom, and (c) top. (d) SKS splitting at the surface resulting from strain-induced LPO computed with the old (left) and new (right) versions of D-Rex; plates are subducting toward the north. The green and orange dashed lines mark, respectively, the trench and the fore-arc/back-arc transition.

between the fixed slab tip lying at the 660 km discontinuity and the upwelling mantle material that is sucked into the mantle wedge.

[33] The poorly deforming slab is nearly isotropic as its geometry is imposed at the beginning of the run, and no LPO can be generated at the mid-ocean ridge.

[34] Synthetic SKS splitting measurements (Figure 4d, right model with white bars) indicate that the fast shear wave component orients parallel to the trench in the outer rise and in the fore arc ($\delta t \leq 1$ s) and perpendicular to it in the back arc ($\delta t = 1$–2.5 s). On the slab sides, the teleseismic fast shear wave component traces the underlying return flow ($\delta t = 1$–2 s). The relatively low delay times of the region seaward and above the fore arc is due to the disruptive interference among layers with different fabrics. Below the slab, in fact, the trench-parallel anisotropy of the lowermost upper mantle is counteracted by the trench-perpendicular anisotropy in the 100 km thick portion of the entrained mantle. Delay times are lower toward the plate center because the divergence of the toroidal flow progressively diminishes producing smaller trench-parallel extension. Trench-parallel delay times are enhanced when the subducting plate is blocked at the rear, thus impeding plate advance (Figure S3). On the other hand, in the back arc, fast shear wave azimuths are mostly oriented trench perpendicular as a result of the constructive interference among the different layers with variably plunging, trench-perpendicular fast axes.

3.2. Models B and C: Large Plate (1000 km Half Width)

[35] The subduction dynamics of a large homogeneous plate (Model B) is similar to that of Model A, except for a smaller retreat of the trench and larger plate advancing. This translates into a larger poloidal flow component that produces a thicker mantle layer entrained at depth with strong trench-perpendicular anisotropy (Figures 5 and S4). In more detail, plate advance causes counterflow in the sub-slab mantle that favors trench-perpendicular anisotropy due to the large velocity gradient between the advancing plate and the lowermost upper mantle that is flowing in the opposite direction [e.g., *Capitanio and Faccenda*, 2012]. The toroidal component of the flow is strongly diverging from the plate midplane near the slab edges causing significant trench-parallel extension and seismic anisotropy similar to that observed in Model A. In the center of the plate, however, divergence of the horizontal flow is minor producing little trench-parallel extension. This is in part due to the boundary conditions used that favor mantle flow through the periodic boundary normal to the x axis rather than return flow around the slab edges. We run a further experiment similar to Model B but without the x-normal periodic boundary. Results

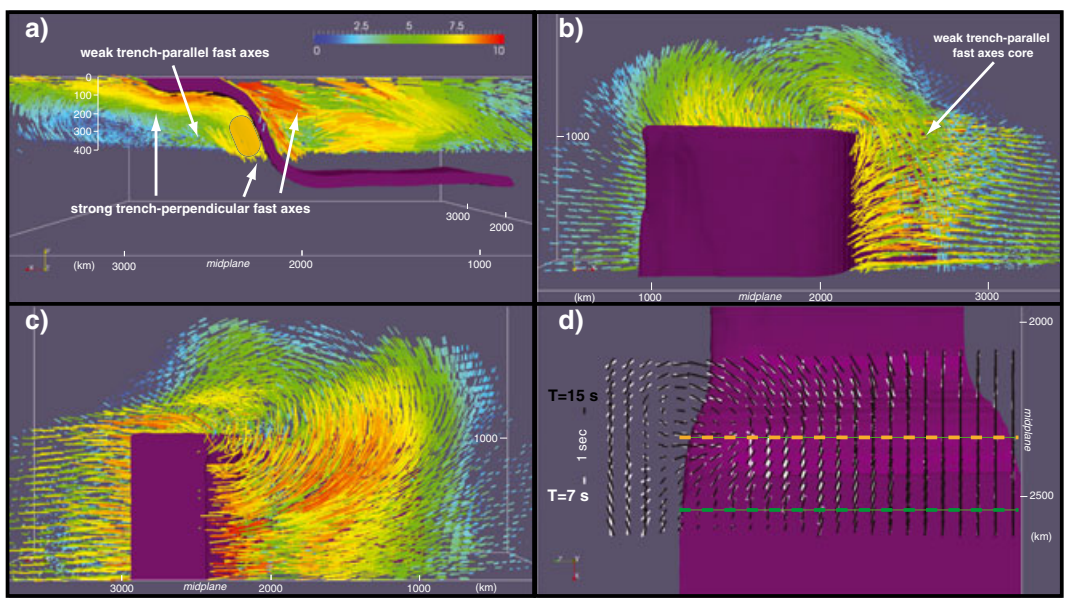

Figure 5. Seismic anisotropy of Model B with a homogeneous, 2000 km wide oceanic plate. Plane view from the (a) midplane, (b) bottom, and (c) top. (d) SKS splitting at the surface calculated with dominant SKS period of 7 s (white bars) and 15 s (black bars). The green and orange dashed lines mark, respectively, the trench and the fore-arc/back-arc transition. The area highlighted in pale orange in the entrained sub-slab mantle in Figure 5a has a strong dip-parallel anisotropy plotted in Figure 10.

(not shown here) show that although slightly higher trench-parallel extension is produced in the sub-slab mantle, subduction is accommodated by larger plate advance when compared to Model B, thus increasing the poloidal component of the flow and the dip-parallel trench-perpendicular anisotropy. As a consequence, trench-parallel anisotropy in the lowermost upper mantle is small below the internal part of subducting plates characterized by weakly diverging toroidal flow and small trench-parallel extension. Similarly to Model A, the fast seismic directions align sub-parallel to the toroidal flow on the slab sides and perpendicular to the trench in the mantle wedge because of trench-normal extension induced by slab roll back.

[36] The azimuths of the fast SKS wave are oriented mostly trench perpendicular in the fore arc and back arc, except near the edge of the plate where they tend to rotate toward the trench strike in the last 100–200 km of trench. On the side of the oceanic plate, the azimuths are sub-parallel to the return flow at depth.

[37] Subduction zones often exhibit a curvature of the trench that is ascribable to, for example, along-trench variation of the plate age [*Morra et al.*, 2006; *Capitanio et al.*, 2011]. Such curvature may, in turn, induce along-trench extension and lateral pressure gradients [*Kneller and van Keken*, 2008; *Capitanio and Faccenda*, 2012]. In order to reproduce more Earth-like subduction geometries, we run a model with a large (2000 km wide) subducting plate whose thickness linearly decreases from 80 km in the midplane to 50 km on both sides (Model C, Figure 6). The model evolution is quite similar to Model B, except that the along-trench variation of the plate thickness induces differential retreat that is more pronounced on the thicker plate center.

[38] The upper mantle fabric is similar to that of Model B, with a strongly anisotropic fast axes that tend to align parallel to the plate motion, while those in the lower part of the upper mantle exhibit mostly a weak trench-parallel anisotropy (although slightly higher than in Model B due to the more diverging toroidal flow). This causes the fast SKS component to be aligned trench perpendicular along the trench, except near the slab edges, and parallel to the return flow at depth along the sides of the subduction zones. The plate curvature induces an additional component of mantle simple shear deformation that translates into a broader region with significant mantle anisotropy on the side of the subduction zone (Figure 6c) when compared with that of Model B (Figure 5c). We note also that delay times in the fore arc are smaller compared to those of Model B. This is due to the higher dip of the slab that induces a sub-vertical tilting of the fast seismic directions in the entrained mantle. As a consequence, vertically incident SKS waves would propagate along the olivine *a* axis, yielding minimum splitting.

3.3. Olivine LPOs and Pressure-induced Fabric Transitions

[39] In addition to the seismic anisotropy obtained with A-type olivine, we tested different olivine

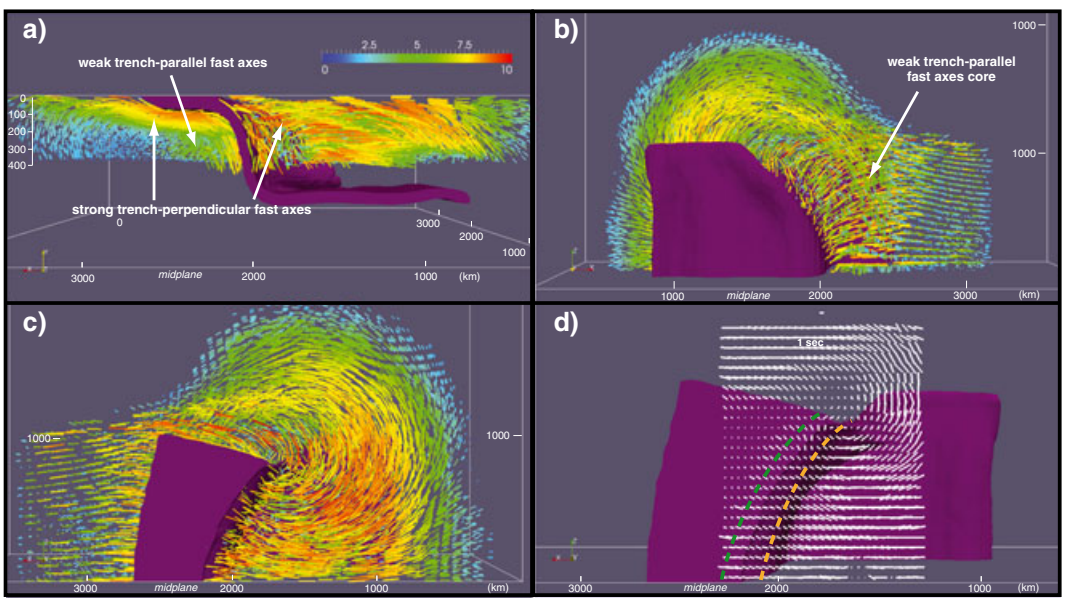

Figure 6. Same as Figure 5 but for Model C.

LPOs (B, C, E type) in order to be able to reproduce SKS splitting patterns observed at subduction zones with a large subducting plate similar to that of Model B (see Supporting Information). In the entrained mantle where dip-parallel simple shear dominates, fast axes are slab parallel (E type), trench parallel (B type), or slab normal (C type) (Figure 7, left column). Fast axes are trench parallel (E type) or varying from sub-vertical to trench perpendicular (B and C type) in the lowermost sub-slab mantle. On the slab side, where the toroidal component of the flow is dominant, fast axes are either parallel (E type) or perpendicular to the flow (B and C type). Fast axes are trench perpendicular (E type), trench parallel (C type), or sub-vertical (B type) in the whole mantle wedge. In summary, E-type LPO give similar orientations of fast directions to those obtained using A-type LPO (Figure 5), while B- and C-type LPOs yield significantly different mantle fabrics.

[40] SKS splitting models show that B-type LPO produces trench-parallel anisotropy, while C and E type yield trench-perpendicular anisotropy (Figure 7, right column).

[41] We also tested SKS splitting in mantle fabric models taking into account two suggested pressure-induced fabric transitions (see Supporting Information). Similarly to the model where the whole upper mantle is assumed to deform with B-type LPO, A- to B-type fabric transition around 90 km depth [*Jung et al*., 2009] yields trench-parallel azimuths in the fore arc and back arc but also seaward of the trench where anisotropy is normally observed to be parallel to the plate motion (Figure 8a). *Mainprice et al*. [2005] proposed that around 200 km the transition from A- to C-type fabric could explain the decrease of seismic anisotropy below this depth in intra-oceanic settings. Accounting for this fabric transition yields trench-perpendicular fast shear wave azimuths (Figure 8b).

[42] Measuring the anisotropy with different LPOs allows determining the shear plane orientation and slip direction of the dominant slip system. Indeed, for any crystal aggregate, the average Burgers

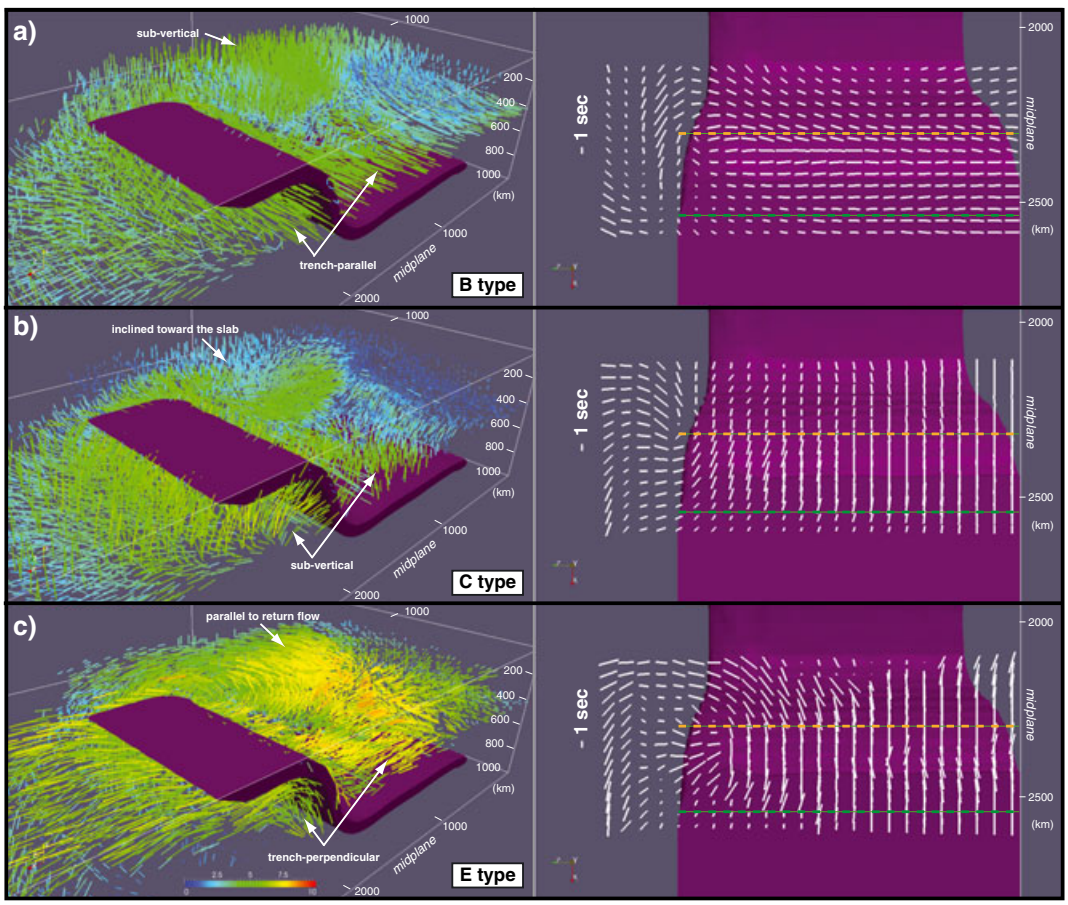

Figure 7. Mantle fabric (left column) and SKS splitting (right column, plane view from the top) calculated for Model B with (a) B-type, (b) C-type, and (c) E-type olivine LPO. The green and orange dashed lines mark, respectively, the trench and the fore-arc/back-arc transition.

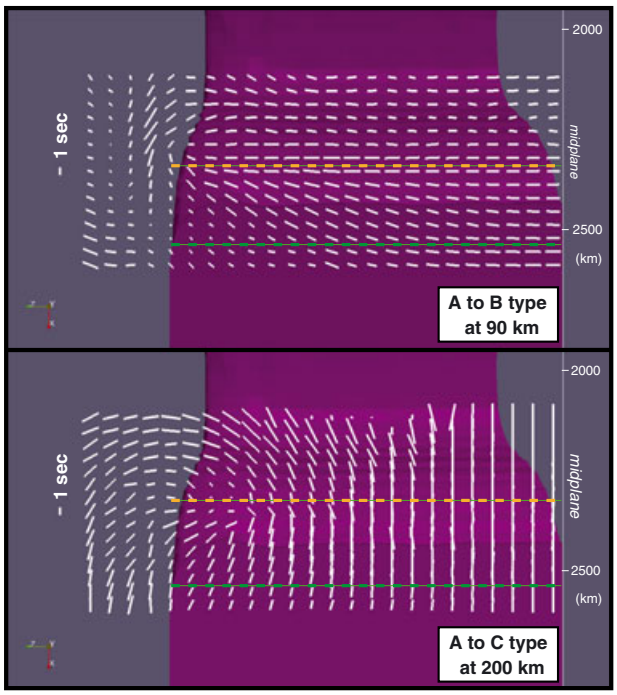

Figure 8. SKS splitting calculated for Model B and resulting from pressure-induced olivine LPO transitions: (a) A- to B-type olivine LPO at 90 km depth [*Jung et al*., 2009] and (b) A- to C-type olivine LPO at 200 km depth [*Mainprice et al*., 2005]. The mantle fabric is not shown, but it can be extrapolated from Figures 5 and 7. Plane view from the top. The green and orange dashed lines mark, respectively, the trench and the fore-arc/back-arc transition.

vector and normal to the slip plane of olivine roughly correspond to the fast axis of, respectively, the A-type (or E-type) LPO and C-type LPO. From the microstructural point of view, the shear plane and slip directions correspond to, respectively, the foliation plane and lineation direction given by the olivine fast axes. In Figure 9, the shear planes normal to the fast axis obtained from Model A with C-type LPO are plotted. The dominant shear planes are mostly sub-vertical in the mantle wedge due to the trench-parallel compression. On the slab edges, the foliation is again sub-vertical but tends to be more inclined toward the slab. This indicates that the mantle velocity gradients are stronger along the radius of the toroidal cell and that return flow is quite homogenous with depth (i.e., $\dot{\varepsilon}_{xz} >> \dot{\varepsilon}_{xy}, \dot{\varepsilon}_{zy}$). In the sub-slab mantle, the orientation of the dominant shear planes varies from sub-vertical oceanward to sub-horizontal below the fore arc, where pure shear deformation dominates. Finally, dip-parallel foliation forms in the entrained mantle.

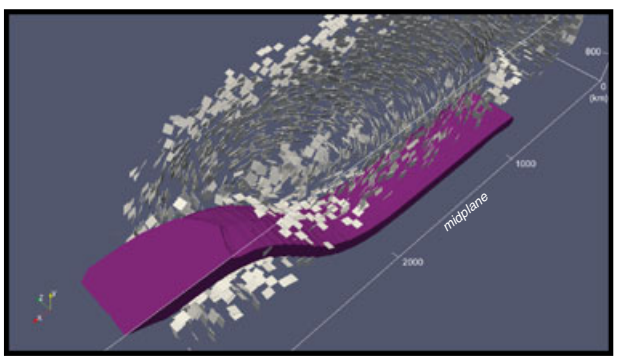

Figure 9. Orientation of the dominant shear plane for olivine crystals estimated for selected mineral aggregates of Model A. The foliation is parallel to these planes. The average Burgers vector is indicated by the fast axis obtained with A-type olivine LPO (Figures 3 and 4).

4. Discussion

4.1. Results Summary and Comparison With Other Studies

[43] The 3-D seismic anisotropy patterns of dynamic subduction models present some interesting features that may help in reconciling part of the global SKS splitting data with the upper mantle flow patterns. In the following discussion, we assume A-type LPO for the whole upper mantle.

[44] High anisotropy is formed in the entrained mantle above and beneath the slab due to simple shear deformation with the dip-parallel fast directions. Similarly to that found by *McKenzie* [1979], we note that the anisotropy and deformation on top of the slab (10%, $f = 4$) are larger than those on the bottom (5–7%, $f < 2$) and progressively decreases away from the slab boundaries. Around steeper slabs, the anisotropy on top of the slab decreases while it increases at the bottom.

[45] Below the slab, the mantle fabric is characterized by two stacked domains with orthogonally oriented fast seismic directions. In the upper domain, a mantle layer is entrained at depth by the subducting plate with strong dip-parallel, trench-perpendicular anisotropy due to simple shear deformation. The thickness of the upper domain increases for models with large and/or advancing plates where trench-perpendicular counterflow patterns establish, thus favoring simple shear deformation, trench-perpendicular anisotropy, and SKS fast azimuths parallel to plate motions. On the other hand, the lower domain is characterized by pure shear deformation due to slab rollback and trench-parallel extension causing trench-parallel anisotropy proportional to the horizontal divergence of the toroidal flow component. For large plates, however, trench-parallel anisotropy in the lower

sub-slab domain is weak except near the external 100–200 km portions of the plates where the toroidal flow is strongly diverging. The curved geometry of the trench enhances diverging toroidal flow and trench-parallel extension. We have calculated the SKS splitting also for models with 1000 and 1400 km wide, homogeneous oceanic plates (not shown here) and found that their seismic anisotropy patterns are similar to those of Model B. This indicates that for relatively large plates (≥500 km half width), SKS splitting patterns are systematic, with fast azimuths in the fore arc being mostly trench perpendicular and rotating toward the trench only in the external 100–200 km portions. Narrower plates (≤300 km half width), instead, subduct preferentially by retreating maximizing pure deformation in the lower sub-slab domain. Here, the LPO strength of the sub-slab lower domain increases progressively toward a strongly anisotropic core with up to 9% transverse anisotropy leading to trench-parallel SKS anisotropy. These patterns are enhanced when the subducting plate is blocked at the rear, thus impeding plate advance. In the more general case, however, as SKS waves are more sensitive to the anisotropy in the shallowest layers [*Schulte-Pelkum and Blackman*, 2003], the entrained mantle layer with trench-perpendicular anisotropy seems to control the anisotropy in the fore arc. Consequently, trench-parallel SKS splitting is observed in the fore arc only for models with relatively narrow plates where retreating motions are maximized and, thus, develop a weaker trench-perpendicular anisotropy in the entrained mantle.

[46] The trench-parallel anisotropy found in the lower domain can be partly reconciled with the results of [*Buttles and Olson*, 1998] that conducted analogue experiments of a retreating plate with no down-dip motion and used whiskers as an analogue of the olivine *a* axis to determine the sub-slab mantle fabric. In their models, the mantle anisotropy field beneath the slab is divided in three zones: zone 1, the closest to the slab, has a weak trench-parallel anisotropy. The intermediate area, zone 2, is characterized by strong trench-parallel alignment of the whiskers that is a function of the amount of retreat. Zone 3, the more distant, is nearly isotropic. On the plate sides, the whiskers align with the toroidal flow. Zone 2 of their analogue models resembles quite well the area with trench-parallel fast axis of our Model A (Figures 3 and 4). The differences concerning zone 1 are attributable to the down-dip motion and non-Newtonian mantle rheology that in our models produce dip-parallel alignment of the fast axis in a layer whose thickness is less than 1/6 of the plate width instead of 1/4. They also conducted an experiment with simultaneous retreat and down-dip motion of a vertical plate and found that the trench-parallel whisker alignment is reduced seaward of the plate. The kinematic of this last experiment is more consistent with our models and with real subduction systems, confirming that the down-dip motion produces trench-perpendicular anisotropy at the expense of the deeper trench-parallel anisotropy.

[47] In all models, the fast SKS waves at the edges of the subduction zones orient sub-parallel to the underlying return flow accommodated by simple shear deformation. On the other hand, in the mantle wedge, the direction of the fast axes and that of the maximum stretching are systematically perpendicular to the trench yielding trench-normal SKS anisotropy with delay times of 1–3 s, no matter of the trench geometry (Figures 5 and 6). Such an orientation is the combined result of simple shear due to poloidal flow and pure shear extension parallel to the direction of trench retreat. In contrast, *Kneller and van Keken* [2008] showed that the curvature of the slab may induce rotation of the maximum stretching axis toward the trench strike in proximity of the mantle wedge corner. This discrepancy can arise for two reasons: first of all, our models may not be able to resolve properly the mantle wedge corner because of the relatively low resolution of the Eulerian grid we used (40 km and 15 km along the horizontal and vertical directions, respectively) compared to that of *Kneller and van Keken* [2008] ranging from 2 to 15 km; in this case, however, the extent of the region with trench parallel anisotropy that would eventually form is so small that would minimally affect the total SKS splitting. Second, the kinematic and geometrically steady-state models of *Kneller and van Keken* [2008] cannot account for the trench-perpendicular pure shear extension that develops above the retreating slab in our dynamic and non-steady-state simulations. The additional trench-perpendicular stretching due to slab rollback impedes the rotation toward the trench strike of the maximum stretching axis in the mantle wedge corner that could be obtained, instead, for subduction models with a fix trench position.

4.2. Comparison of the Synthetic Patterns of Anisotropy With Observations and Implications for the Flow and Fabric in the Upper Mantle

[48] The subduction flow models are characterized by retreat of a single oceanic plate favored by the

absence of a stiff overriding plate. It follows that the results of our models are mostly applicable to subduction zones characterized by a discrete amount of retreat in the recent history and with no other subducting slabs in close proximity. *Faccenda and Capitanio* [2012] showed that the magnitude of anisotropy and SKS delay times are function exclusively of the amount of plate subduction and are independent of the rate at which the slab subducts/retreats. This result is consistent with laboratory experiments, numerical and analytical solutions indicating that as long as dislocation creep dominates, the strength of the LPO is related to the finite strain and not strain rate [*Ribe*, 1992; *Zhang and Karato*, 1995; *Buttles and Olson*, 1998; *Bystricky et al*., 2000]. Hence, our predictions are independent of kinematic indicators like trench migration rates or subduction velocities that are commonly used to characterize the dynamic behavior of a subduction system [e.g., *Heuret and Lallemand*, 2005]. The only exception is represented by the dimensionless subduction partitioning ratio SPR = $v_{SP}/(v_{SP} + v_T)$, where v_{SP} and v_T are the trench-normal subducting plate and trench migration velocities, respectively [*Schellart et al*., 2011]. Retreating plates with low SPR would favor trench-parallel anisotropy in the lower sub-slab domain against trench-perpendicular fabric in the upper sub-slab domain that, in contrast, is produced by plate advancing. Indeed, time delays with trench-parallel fast azimuths in the fore arc are higher in models with a narrow plate blocked at the rear (Figure S3) compared to those where no kinematic boundary conditions are imposed (Figure 4d). Low SPRs would additionally induce strong return flow at subduction zone edges and trench-perpendicular extension in the mantle wedge, thus enhancing fast directions oriented, respectively, sub-parallel to the toroidal component of the flow and normal to the trench.

[49] Having discussed the dynamic and kinematic constrains for the applicability of the models to natural subduction settings and their implications in terms of the upper mantle fabric, we now pass to compare in more detail the synthetic SKS splitting patterns with the observations.

[50] SKS fast azimuths at the lateral edges of the subduction zone align in a circular pattern and are sub-parallel to the underlying return flow in all models. This pattern is consistent with the observations in Calabria [*Civello and Margheriti*, 2004], Cascadia [*Zandt and Humphreys*, 2008], and possibly southeast of Alboran [*Diaz et al*., 2010] where retreat has occurred in the last 20–30 Ma, proving, as previously suggested, that in these regions the upper mantle below the slab is flowing in the mantle wedge to accommodate the retreat.

[51] SKS fast wave azimuths are oriented parallel to the plate motions right above the oceanic plate lateral boundaries at the surface in Model B-C where significant plate advance induces strike-slip deformation. The same patterns are observed in Kamchatka where trench-normal fast directions are parallel to the transform fault on the northern edge of the subducting Pacific plate [*Peyton et al*., 2001]. In real settings, such pattern is likely enhanced by plasticity active at shallow depths in the transform faults that help in focusing strain, increasing the trench-normal anisotropy along the subduction zones boundaries.

[52] In the arc and back-arc regions, trench-normal synthetic SKS anisotropy with delay times of 1–2.5 s is systematically found. This is consistent with those observed in the back arc of retreating Tonga, Cascadia, and Mediterranean subduction systems [*Smith et al*., 2001; *Zandt and Humphreys*, 2008; *Jolivet et al*., 2009], except for slightly higher synthetic delay times. According to the flow models, this implies that in these tectonic settings, the mantle above the slab is flowing sub-horizontally parallel to the retreating direction. There are dynamic processes that may weaken the synthetic anisotropic patterns. For example, the sub-horizontal mantle flow may be disturbed by delamination of the overriding lithosphere [*Levander et al*., 2011]. In the volcanic arc region, fast azimuth directions are variable from slab parallel to slab perpendicular [e.g., *Baccheschi et al*., 2007]. Here, the interpretation of SWS patterns is not straightforward as the mantle flow is likely perturbed by the rising of chemically buoyant plumes [*Zhu et al*., 2009] and possibly by the foundering of the lower crust [*Behn et al*., 2007]. Additional complications may arise due to presence of melt pockets/bands [*Holtzman et al*., 2003]. As a consequence, synthetic delay times in the arc and back-arc regions must be considered as an upper bound.

[53] Trench-parallel SKS anisotropy is widely observed at most subduction zone fore arcs [*Long and Silver*, 2009]. However, synthetic fast azimuths are trench parallel only for narrow plates with low SPR (Figures 4d and S3) and on the margins of larger subduction zones, while they tend to align trench perpendicular in all other cases. We discuss in greater detail such discrepancy in section 4.3.

[54] In our models, the oceanic plate is nearly isotropic through the whole model run. Despite

the difficulty in studying this area that is embedded in between two strongly anisotropic mantle layers, slab anisotropy has been detected or suggested in several subduction systems [*Anglin and Fouch*, 2005; *Brisbourne et al*., 1999; *Hammond et al*., 2010; *Huang et al*., 2011; *Pidgeon and Savage*, 1997; *Ishise and Oda*, 2005; *Vavrycuk*, 2005]. Slab anisotropy has been interpreted as formed by flow at spreading centers inducing sub-horizontal, ridge-normal fast directions in the oceanic lithosphere [*Blackman and Kendall*, 2002; *Kaminski and Ribe*, 2002] or by serpentinized/fluid-filled fractures that are activated during bending at the trench outer rise [*Faccenda et al*., 2008] and wetted by dehydration at intermediate depths [*Faccenda et al*., 2012]. In the first case, the fossil slab anisotropy is mainly dip parallel because the strike of most subduction zones is parallel to that of mid-ocean ridges, while in the second case, the slab fabric could be approximated with a transversely isotropic layer with a trench-normal, slow symmetry axis. With respect to the observed trench-parallel anisotropy in most fore arcs, the slab fossil fabric is considered to interfere disruptively when the magnetic lineations of the seafloor are trench parallel, while the bending faults will interfere positively and, moreover, would explain the frequency dependency observed in some datasets [*Pidgeon and Savage*, 1997; *Huang et al*., 2011]. We note that, however, according to the recent model of *Song and Kawakatsu* [2012], the negative interference of the fossil fabric in the tilted slab could be reevaluated.

[55] The distribution of the anisotropy in the mantle reflects the distribution of the deformation. Indeed, the upper mantle fabric is strong near the subduction zone down to 410 km depth where deformation is high and vanishes away from it. This is consistent with the strong anisotropy found down to the 410 km discontinuity at subduction zones [e.g., *Fouch and Fischer*, 1996; *Mueller et al*., 2008; *Foley and Long*, 2011; *Di Leo et al*., 2012]. Seaward of the trench, strong fabric is present down to about 200 km depth in the intra-oceanic portion of the oceanic plate. On Earth, the Lehmann discontinuity and the decrease of seismic anisotropy from 200 to 300 km depth, where the mantle appears to be isotropic, found in intra-oceanic settings [*Dziewonski and Anderson*, 1981; *Montagner and Tanimoto*, 1991] were interpreted as due to either a transition between an anisotropic uppermost mantle deforming by dislocation creep and an isotropic deep mantle deforming by diffusion creep [*Karato*, 1992] or, alternatively, to pressure-induced fabric transition from A- to C-type LPO [*Mainprice et al*., 2005]. While either diffusion creep or static recrystallization (annealing) may be active in the poorly and slowly deforming deeper portions, we interpret these observations as a natural consequence of the non-Newtonian behavior of the viscous upper mantle where the deformation due to motions of the overlying plates is not homogeneously distributed (i.e., Couette flow) but concentrates at shallow depths [i.e., *Tommasi*, 1998]. Near the rear of the plate, medium to strong anisotropy is found down to the base of the upper mantle where upwelling and diverging flow reproduces deformation at mid-ocean ridges. It is important to note that such distribution of the mantle fabric can only be obtained with the modified version of D-Rex, while the steady-state version would produce strong anisotropy in the whole mantle (Figure 4).

4.3. The Quest for the Source of Trench-Parallel Anisotropy in Fore Arcs

[56] Trench-parallel SKS anisotropy is observed at 90% of the global fore arcs with sub-wedge delay times that appears to be proportional to the migration velocity of the trench [*Long and Silver*, 2009]. Our results show that only models with a narrow and retreating slab are able to explain trench-parallel fast azimuths in the fore arc at geometrically and kinematically similar subduction settings like Calabria, South Sandwich, and Alboran (and possibly Caribbean) where a small slab is attached to a much larger, non-subducting plate, maximizing retreat motions (Figures 4d and S3). On the other hand, models with advancing and/or large plates yield mostly trench-perpendicular SKS splitting patterns. This discrepancy can be diminished either by

1. Running thermo-mechanical models with a higher numerical resolution and more realistic, temperature- and pressure-dependent viscous rheologies. In this way, thermal and mechanical feedbacks will act to reduce the thickness of the layer beneath the oceanic plate with trench-perpendicular anisotropy. This mechanism is similar to what has been proposed by *Long and Silver* [2009] for sub-slab mantle decoupling from the entrained flow but does not necessarily imply trench-parallel flow beneath the slab.
2. Introducing more complex lower and upper plate geometries, along-trench variations in the mantle compositions [*Hall et al*., 2000; *Capitanio and Faccenda*, 2012] that, together with that discussed in the previous point, could lead to trench-parallel flow [*Russo and Silver*, 1994].
3. Introducing an additional, trench-parallel anisotropic source in the mantle wedge. Local *S* waves

splitting data suggest that the mantle wedge corner below the fore arc is characterized in many cases by trench-parallel anisotropy, although frequently with smaller delay times than those measured with SKS waves [*Long and Becker*, 2010]. This can be explained with the presence of water that may lead to the formation of B-type olivine at relatively high-T condition and high stresses [*Kneller et al*., 2005] or of hydrous phases at low-T conditions. Highly anisotropic hydrous phases such as serpentine, amphibole, and talc [*Kern et al*., 1997; *Mainprice*, 2007; *Watanabe et al*., 2007] may indeed be present directly above the dehydrating slab [*Katayama et al*., 2009] or in the cold nose of the mantle wedge [*Mookherjee and Capitani*, 2011; *Kneller et al*., 2008]. Other complications may arise from structures with a shape preferred orientation (SPO) like fluid-filled cracks right above the slab [*Healy et al*., 2009].

4. Introducing an additional, trench-parallel anisotropic source in the slab at intermediate depths [e.g., *Faccenda et al*., 2008].

[57] Alternatively, we have shown that by assuming B-type olivine LPO for the upper mantle, trench-parallel anisotropy is calculated in the fore arc of relatively large plates. However, B-type fabric would yield fast azimuths perpendicular to plate motions in intra-oceanic settings and mid-oceanic ridges, inconsistently with the observed azimuthal anisotropy [e.g., *Montagner and Tanimoto*, 1991]. Considering that the sharp (<10 km wide) 410 km discontinuity that is commonly (but not uniquely) observed, the degree of melting of N-MORB source rocks [*Wood and Corgne*, 2007] and electrical conductivity surveys [*Wang et al*., 2006] suggests a relatively dry upper mantle (A- or E-type LPO according to *Karato et al*. [2008]); we therefore conclude that B-type fabric cannot be widely present in the upper mantle.

[58] Recently, *Song and Kawakatsu* [2012] proposed an alternative model for the interpretation of the observed trench-parallel anisotropy based on the orthorhombic elastic symmetry of the asthenosphere. In intra-oceanic settings, azimuthal (A_S) and radial (R_S) anisotropy with, respectively, fast directions aligned parallel to the plate motions and $V_{SH}>V_{SV}$ (where V_{SH} and V_{SV} are the horizontally (Love) and vertically (Rayleigh) polarized surface waves) are found to approximately 200 km of depth [*Dziewonski and Anderson*, 1981; *Montagner and Tanimoto*, 1991]. The foliation plane and the lineation direction in the shearing asthenosphere are always dip parallel, being horizontal in intra-oceanic settings and tilted below the slab. For a horizontal asthenosphere, the azimuth of the vertically traveling, fast SKS wave component is a function exclusively of A_S, aligning parallel to the lineation and plate motion directions. For an asthenosphere oriented sub-vertically, instead, the azimuth of the fast SKS component depends exclusively on R_S, aligning parallel to the foliation plane and perpendicular to plate motion (in this case, however, delay times would be small as SKS waves would propagate parallel to the lineation, i.e., the olivine fast axis). By using $R_s=3\%$, $A_s=2\%$, and the ellipticity $\eta=0.95$, values that are in the range of those observed [*Song and Kawakatsu*, 2012] showed that the fast SKS wave should orient parallel to the trench in the fore arc above slabs dipping more than 23°. It is worth noting that by using a slightly different combination of R_s, A_s, and η no trench-parallel anisotropy is produced, implying that caution must be taken when considering this mechanism. Nevertheless, according to our models with relatively large plates where the fabric of the entrained asthenosphere controls the SKS splitting patterns, this new interpretation seems to be plausible. In our models, the fabric of the entrained asthenosphere, although having orthorhombic symmetry (Figure 10), yields trench-perpendicular anisotropy even for a highly dipping slab like that of Model B (Figure 5). Table S2 shows the elastic moduli of the entrained sub-slab mantle rotated by 50° in the horizontal plane. In this layer, $R_S=5.7\%$ is similar to $A_S=5.4\%$, both being higher than those used by *Song and Kawakatsu* [2012], while the $\eta=0.79$ is lower than those measured on Earth (0.9–1.0) [e.g., *Dziewonski and Anderson*, 1981]. This suggests that while a first-order approximation of the upper mantle fabric is achieved, the modeled LPO in the asthenosphere is probably too strong, yielding to an overestimation of the seismic anisotropy. Considering that the creep parameters in D-Rex have been chosen to fit at best the experimental LPOs run at upper mantle P-T conditions [e.g., *Zhang and Karato*, 1995], such an inconsistency rises questions about our understanding of the petrophysical processes behind upper mantle deformation, especially when scaled to geological times.

[59] The relation found by *Long and Silver* [2009] between sub-wedge delay times and trench migration rates is appealing but probably has no physical meaning because the strength of the mantle fabric and sub-wedge δt are independent of the rate at which the slab subducts/retreats [*Faccenda and Capitanio*, 2012]. In order to explain the whole range of data, we speculate that the global average sub-wedge δt is a function of a given primary source of trench-parallel anisotropy and

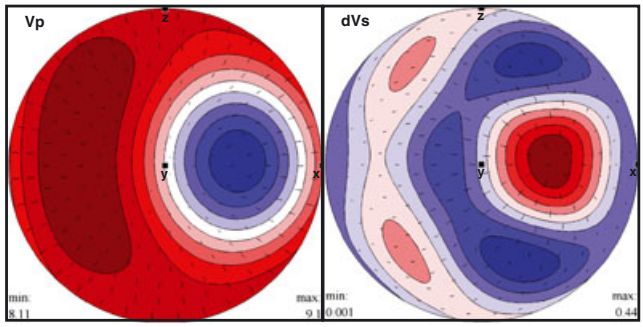

Figure 10. Wave velocities of a crystal aggregate representative of the sub-slab mantle entrained at depth with the slab in Model B (Figure 5a, orange area) plotted in seismic color maps (MTEX) [*Mainprice et al*., 2011]. Upper panel: *P* wave velocities together with *P* wave polarization direction. Lower panel: dVs in s/km together with the S1-wave polarization direction.

that additional anisotropic sources may interfere constructively or destructively with the primary source yielding to, respectively, larger or smaller δt compared to the global average. If we consider the entrained mantle (and possibly in the tilted slab itself) as the primary source of sub-wedge trench-parallel anisotropy in the fore arc, the fabric in the lower sub-slab domain could represent one of the additional anisotropic sources interfering constructively. We note, for example, that some of the sub-wedge delay times above the global average correspond to subduction zones like Tonga, Calabria, and South Sandwich where retreat motions are the greatest.

5. Conclusions

[60] The upper mantle seismic anisotropy developed during tectonic plate subduction and the resulting SKS splitting patterns have been calculated with an integrated numerical modeling of 3D mechanical subduction and induced non-Newtonian mantle flow, strain-induced LPO, and seismic wave propagation by using three existing open source software codes (Underworld, D-Rex, and FSTRACK). D-Rex has been modified to account for a physically consistent, time-dependent development of the strain-induced anisotropy, yielding mantle fabrics that are consistent with the deformation history of non-steady-state, dynamic systems like subduction zones.

[61] We found that the magnitude and distribution of the anisotropy depend on the amount and distribution of the deformation, consistently with laboratory experiments and mineral physics theory. Indeed, although seismic anisotropy is detected down to 200–300 km depth in intra-oceanic settings, at subduction zones strong upper mantle fabric forms down to the 410 km discontinuity with a magnitude of the anisotropy that is proportional to the amount of subduction and is independent of the rate at which the plate subducts.

[62] Plate subduction and retreat induce (1) simple shear deformation in the upper mantle entrained at depth and on the slab edges where return flow takes place and (2) coaxial deformation in the lowermost sub-slab mantle and in the mantle wedge where the maximum extension direction orients, respectively, parallel and perpendicular to the trench. As a consequence, the sub-slab mantle is composed of two domains with different fabrics that control the SKS splitting patterns in the fore arc interfering destructively: the upper domain with trench-perpendicular anisotropy and the lower with trench-parallel alignment of the fast seismic direction. The strength of the lower domain fabric is proportional to the horizontal divergence of the flow and decreases from the slab edges toward the plate center where becoming weak. Plate advance produces to a strong fabric in the upper domain, while slab retreat increases the trench-parallel anisotropy in the lower domain. Except near the plate edges, the upper domain with trench-perpendicular anisotropy has a stronger fabric than the lower domain, yielding fast SKS wave azimuth oriented trench parallel for relatively narrow and retreating slabs ($\leq$600 km wide and low SPR) and trench perpendicular for larger and/or advancing plates.

[63] The anisotropy in the back arc and on the sides of the subducting plate is systematically trench perpendicular and parallel to the return flow at depth, respectively.

[64] Although our model predictions could be improved by including more realistic temperature and pressure dependent rheologies and elastic tensors, and by calculating the strain-induced

LPO of transition zone and lower mantle phases, results from our regional scale models help to infer the flow and composition of the upper mantle by comparison with the wide range of subduction zone seismic data observed globally. Furthermore, although this study focuses on subduction zones, our methodology allows for realistic predictions of the relations between flow in the upper mantle and SKS splitting patterns in any geodynamic setting.

Acknowledgments

[65] This work has been supported by the Australian Research Council *Discovery Projects* DP0987374 and DP110101697 awarded to F.A.C. We are grateful to E. Kaminski and W.P. Schellart for the discussion about D-Rex and the SPR, respectively, and R.J. Farrington for improving the English of the manuscript. We also thank two anonymous reviewers, the associate editor and T.W. Becker, for their constructive review.

References

Anglin, D. K., and M. J. Fouch (2005), Seismic anisotropy in the Izu-Bonin subduction system, *Geophys. Res. Lett.*, *32*, doi:10.1029/2005GL022714.

Baccheschi, P., L. Margheriti, and M. S. Steckler (2007), Seismic anisotropy reveals focused mantle flow around the Calabrian slab (Southern Italy), *Geophys. Res. Lett.*, *34*, doi:10.1029/2006GL028899.

Backus, G. E. (1962), Long-wave elastic anisotropy produced by horizontal layering, *J. Geophys. Res.*, *67*, 4427–4440.

Becker, T. W., J. B. Kellogg, G. Ekström, and R. J. O'Connell (2003), Comparison of azimuthal seismic anisotropy from surface waves and finite strain from global mantle-circulation models, *Geophys. J. Int.*, *155*, 696–714.

Becker, T. W., B. Kustowski, and G. Ekström (2008), Radial seismic anisotropy as a constraint for upper mantle rheology, *Earth Planet. Sci. Lett.*, *267*, 213–227.

Becker, T. W., S. Lebedev, and M. D. Long (2012), On the relationship between azimuthal anisotropy from shear splitting and surface wave tomography, *J. Geophys. Res.*, *117*, doi:10.1029/2011JB008705.

Becker, T. W., V. Schulte-Pelkum, D. K. Blackman, J. B. Kellogg, and R. J. O'Connell (2006), Mantle flow under the western United States from shear wave splitting, *Earth Planet. Sci. Lett.*, *247*, 235–251.

Behn, M. D., G. Hirth, and P. B. Kelemen (2007), Trench-parallel anisotropy produced by foundering of arc lower crust, *Science*, *317*, 108–111.

Blackman, D. K., and J. M. Kendall (2002), Seismic anisotropy in the upper mantle 2. Predictions for current plate boundary flow models, *Geochem. Geophys. Geosyst.*, *3*, doi:10.1029/2001GC000247.

Blackman, D. K., H. R. Wenk, and J.-M. Kendall (2002), Seismic anisotropy of the upper mantle: 1. Factors that affect mineral texture and effective elastic properties, *Geochem. Geophys. Geosyst.*, *9*, doi:10.1029/2001GC000248.

Booth, D. C., and S. Crampin (1985), The anisotropic reflectivity technique: Theory, *Geophys. J. R. Astron. Soc.*, *72*, 31–45.

Brisbourne, A., G. Stuart, and J.-M. Kendall (1999), Anisotropic structure of the Hikurangi subduction zone, New Zealand-integrated interpretation of surface-wave and body-wave observations, *Geophys. J. Int.*, *137*, 214–230.

Browaeys, T. J., and S. Chevrot (2004), Decomposition of the elastic tensor and geophysical applications, *Geophys. J. Int.*, *159*, 667–678.

Buttles, J., and P. Olson (1998), A laboratory model of subduction zone anisotropy, *Earth Planet. Sci. Lett.*, *164*, 245–262.

Bystricky, M., K. Kunze, L. Burlini, and J.-P. Burg (2000), High shear strain of olivine aggregates: Rheological and seismic consequences, *Science*, *290*, 1564–1567.

Capitanio, F. A., and M. Faccenda (2012), Complex mantle flow around heterogeneous subducting oceanic plates, *Earth Planet. Sci. Lett.*, *353–354*, 29–37.

Capitanio, F. A., C. Faccenna, S. Zlotnik, and D. R. Stegman (2011), Subduction dynamics and the origin of Andean orogeny and the Bolivian orocline, *Nature*, *480*, 83–86.

Capitanio, F. A., G. Morra, and S. Goes (2009), Dynamics of plate bending at the trench and slab-plate coupling, *Geochem. Geophys. Geosyst.*, *10*, 1–15, doi:10.1029/2008GC002348.

Chapman, C. H., and P. M. Shearer (1989), Ray tracing in azimuthally anisotropic media: II. Quasishear wave coupling, *Geophys. J. Int.*, *96*, 65–83.

Civello, S., and L. Margheriti (2004), Toroidal mantle flow around the Calabrian slab (Italy) from SKS splitting, *Geophys. Res. Lett.*, *31*(L10601), 1–4.

Conrad, C. P., M. D. Behn, and P. G. Silver (2007), Global mantle flow and the development of seismic anisotropy: Differences between the oceanic and continental upper mantle, *J. Geophys. Res.*, *112*, doi:10.1029/2006JB004608.

Crampin, S. (1994), The fracture criticality of crustal rocks, *Geophy. J. Int.*, *118*, 428–438.

Di Leo, J. F., J. Wookey, J. O. S. Hammond, J.-M. Kendall, S. Kaneshima, H. Inoue, T. Yamashina, and P. Harjadi (2012), Deformation and mantle flow beneath the Sangihe subduction zone from seismic anisotropy, *Phys. Earth Planet. Inter.*, *194–195*, 38–54.

Diaz, J., J. Gallrt, A. Villasenor, F. Mancilla, A. Pazos, D. Cordoba, J. A. Pulgar, P. Ibarra, and M. Harnafi (2010), Mantle dynamics beneath the Gibraltar Arc (western Mediterranean) from shear-wave splitting measurements on a dense seismic array, *Geophys. Res. Lett.*, *37*, doi:10.1029/2010GL044201.

Dziewonski, A. M., and D. L. Anderson (1981), Preliminary reference Earth model, *Phys. Earth Planet. Int.*, *25*, 297–356.

Faccenda, M., L. Burlini, T. V. Gerya, and D. Mainprice (2008), Fault-induced seismic anisotropy by hydration in subducting oceanic plates, *Nature*, *455*, 1097–1100.

Faccenda, M., and F. A. Capitanio (2012), Development of mantle seismic anisotropy during subduction-induced 3-D flow, *Geophys. Res. Lett.*, *39*, 11, doi:10.1029/2012GL051988.

Faccenda, M., T. V. Gerya, N. S. Mancktelow, and L. Moresi (2012), Fluid flow during slab unbending and dehydration: Implications for intermediate-depth seismicity, slab weakening and deep water recycling, *Geochem. Geophys. Geosyst.*, *13*, doi:10.1029/2011GC003860.

Foley, B. J., and M. D. Long (2011), Upper and mid-mantle anisotropy beneath the Tonga slab, *Geophys. Res. Lett.*, *38*, doi:10.1029/2010GL046021.

Fouch, M. J., and M. Fischer (1996), Mantle anisotropy beneath northwest Pacific subduction zones, *J. Geophys. Res.*, *101*, 15987–16002.

Funiciello, F., M. Moroni, C. Piromallo, C. Faccenna, A. Cenedese, and H. A. Bui (2006), Mapping mantle flow during retreating subduction: Laboratory models analyzed by feature tracking, *J. Geophys. Res.*, *111*, doi:10.1029/2005JB003792.

Hall, C. E., K. Fisher, E. M. Parmentier, and D. K. Blackman (2000), The influence of plate motions on three-dimensional back arc mantle flow and shear wave splitting, *J. Geophys. Res.*, *105*, 28,009–28,033.

Hammond, J. O. S., J. Wookey, S. Kaneshima, H. Inoue, T. Yamashina, and P. Harjadi (2010), Systematic variation in anisotropy beneath the Mantle wedge in the Java-Sumatra subduction system from shear-wave splitting, *Phys. Earth Planet. Int.*, *178*, 189–201.

Healy, D., S. M. Reddy, N. E. Timms, E. M. Gray, and A. V. Brovarone (2009), Trench-parallel fast axes of seismic anisotropy due to fluid-filled cracks in subducting slabs, *Earth Planet. Sci. Lett.*, *283*, 75–86.

Heuret, A., and S. Lallemand (2005), Plate motions, slab dynamics and back-arc deformation, *Phys. Earth Planet. Inter.*, *149*, 31–51.

Hirth, G., and D. L. Kohlstedt (2003), Rheology of the upper mantle and the mantle wedge: A view from the experimentalists, in Inside the Subduction Factory, vol. 138, Anonymouss, pp. 83–105, Geophysical Monograph American Geophysical Union, Washington D. C.

Holtzman, B. K., D. L. Kohlstedt, M. E. Zimmerman, F. Heidelbach, T. Hiraga, and J. Hustoft (2003), Melt Segregation and Strain Partitioning: Implications for Seismic Anisotropy and Mantle Flow, *Science*, *301*, 1227–1230.

Huang, Z., D. Zhao, and L. Wang (2011), Frequency-dependent shear-wave slitting and multilayer anisotropy in northeast Japan, *Geophys. Res. Lett.*, *38*, doi:10.1029/2010GC003343.

Ishise, M., and H. Oda (2005), Three-dimensional structure of *P*-wave anisotropy beneath the Tohoku district, northeast Japan, *J. Geophys. Res.*, *110*, doi:10.1029/2004JB003599.

Jadamec, M. A., and M. I. Billen (2010), Reconciling surface plate motions with rapid three-dimensional mantle flow around a slab edge, *Nature*, *465*, 338–341.

Jolivet, L., C. Faccenna, and C. Piromallo (2009), From mantle to crust: Stretching the Mediterranean, *Earth Planet. Sci. Lett.*, *285*, 198–209.

Jung, H., W. Mo, and H. W. Green (2009), Upper mantle seismic anisotropy resulting from pressure-induced slip transition in olivine, *Nat. Geo.*, *2*, 73–77.

Kaminski, E., and N. M. Ribe (2002), Timescales for the evolution of seismic anisotropy in mantle flow, *Geochem. Geophys. Geosyst.*, *3*, 1051, doi:10.1029/2001GC000222.

Kaminski, E., N. M. Ribe, and T. Browaeys (2004), D-Rex, a program for calculation of seismic anisotropy due to crystal lattice preferred orientation in the convective upper mantle, *Geophys. J. Int.*, *158*, 744–75.

Karato, S. (1992), On the Lehman discontinuity, *Geophys. Res. Lett.*, *19*, 2255–2258.

Karato, S., H. Jung, I. Katayama, and P. Skemer (2008), Geodynamic significance of seismic anisotropy of the upper mantle: New insights from laboratory studies, *Ann. Rev. Earth Planet. Sci.*, *36*, 59–95.

Karato, S., and P. Wu (1993), Rheology of the upper mantle: A synthesis, *Science*, *260*, 771–778.

Karato, S.-I., M. R. Riedel, and D. A. Yuen (2001), Rheological structure and deformation of subducted slabs in the mantle transition zone: Implications for mantle circulation and deep earthquakes, *Phys. Earth Planet. Inter.*, *127*, 83–108.

Katayama, I., K. Hirauchi, K. Michibashi, and J. Ando (2009), Trench-parallel anisotropy produced by serpentine deformation in the hydrated mantle wedge, *Nature*, *461*, 1114–1117.

Kawazoe, T., S. Karato, K. Otsuka, Z. Jing, and M. Mookherjee (2009), Shear deformation of dry polycrystalline olivine under deep upper mantle conditions using a rotational Drickamer apparatus (RDA), *Phys. Earth Planet. Inter.*, *174*, 128–137.

Kennett, B. L. N. (1983), Seismic Wave Propagation in Stratified Media, Cambridge Univ. Press, New York.

Kern, H., B. Liu, and T. Popp (1997), Relationship between anisotropy of *P* and *S* wave velocities and anisotropy of attenuation in serpentinite and amphibolite, *J. Geophys. Res.*, *102*, 3051–3065.

Kneller, E. A., M. D. Long, and P. E. van Keken (2008), Olivine fabric transitions and shear wave anisotropy in the Ryukyu subduction system, *Earth Planet. Sci. Lett.*, *268*, 268–282.

Kneller, E. A., and P. E. van Keken (2008), Effect of three-dimensional slab geometry on deformation in the mantle wedge: Implications for shear wave anisotropy, *Geochem. Geophys. Geosyst.*, *9*, doi:10.1029/2007GC001677.

Kneller, E. A., P. E. van Keken, S.-I. Karato, and J. Park (2005), B-type olivine fabric in the mantle wedge: Insights from high-resolution non-Newtonian subduction zone models, *Earth Planet. Sci. Lett.*, *237*, 781–797.

Kohlstedt, D. L., B. Evans, and S. J. Mackwell (1995), Strength of the lithosphere: Constrains imposed by laboratory experiments, *J. Geophys. Res.*, 17,587–17,602.

Lassak, T. M., M. J. Fouch, C. E. Hall, and E. Kaminski (2006), Seismic characterization of mantle flow in subduction systems: Can we resolve a hydrated mantle wedge? *Earth Planet. Sci. Lett.*, *243*, 632–649.

Levander, A., B. Schmandt, M. S. Miller, K. Liu, E. K. Karlstrom, R. S. Crow, C.-T. A. Lee, and E. D. Humphreys (2011), Continuing Colorado plateau uplift by delamination-style convective lithospheric downwelling, *Nature*, *472*, 461–465.

Long, M. D., and T. W. Becker (2010), Mantle dynamics and seismic anisotropy, *Earth Planet. Sci. Lett.*, *297*, 341–354.

Long, M. D., B. H. Hager, M. V. de Hoop, and R. D. van der Hilst (2007), Two-dimensional modelling of subduction zone anisotropy with application to southwestern Japan, *Geophys. J. Int.*, *170*, 839–856.

Long, M. D., and P. G. Silver (2009), Mantle flow in subduction systems: The subslab flow field and implications for mantle dynamics, *J. Geophys. Res.*, *114*, doi:10.1029/2008JB006200.

Mainprice, D. (1990), Phase transformation and inherited lattice preferred orientations: Implications for seismic properties, *Tectonophysics*, *180*, 213–228.

Mainprice, D. (2007), Seismic anisotropy of the deep Earth from a mineral and rock physics perspective in, Treatise of Geophysics, vol. *2*, edited by Schubert, G., pp. 437–492, Elsevier, Oxford.

Mainprice, D., R. Hielscher, and H. Schaeben (2011), Calculating anisotropic physical properties from texture data using the MTEX open source package, in Deformation Mechanisms: Rheology and Tectonics: Microstructures, Mechanics and Anisotropy, vol. *360*, edited by D. J. Prior, E. H. Rutter, and D. J. Tatham, pp. 175–192, Geological Society, London.

Mainprice, D., A. Tommasi, H. Couvy, P. Cordier, and D. J. Forst (2005), Pressure sensitivity of olivine slip systems and seismic anisotropy of Earth's upper mantle, *Nature*, *433*, 731–733.

Masalu, D. C. P. (2007), Mapping absolute migration of global mid-ocean ridges since 80 Ma to Present, *Earth Planets Space*, *59*, 1061–1066.

McKenzie, D. (1979), Finite deformation during fluid flow, *Geophys. J.R. Astron. Soc.*, *58*, 689–715.

Menke, W., and V. Levin (2003), The cross-convolution method for interpreting SKS splitting observations, with

application to one and two layer anisotropic earth models, *Geophys. J. Int.*, *154*, 379–392.
Miller, M. S., and T. W. Becker (2012), Mantle flow deflected by interactions between subducted slabs and cratonic keels, *Nat. Geo.*, *5*, 726–730.
Montagner, J. P., and T. Tanimoto (1991), Global upper mantle tomography of seismic velocities and anisotropies, *J. Geophys. Res.*, *96*, 20,337–20,351.
Monteiller, V., and S. Chevrot (2011), High-resolution imaging of the deep anisotropic structure of the San Andreas Fault system beneath southern California, *Geophys. J. Int.*, *186*, 418–446.
Mookherjee, M., and G. C. Capitani (2011), Trench parallel anisotropy and large delay times: Elasticity and anisotropy of antigorite at high pressures, *Geophys. Res. Lett.*, *38*, doi:10.1029/2011GL047160.
Moresi, L., S. Quenette, V. Lemiale, C. Meriaux, B. Appelbe, and H. B. Muehlhaus (2007), Computational approaches to studying non-linear dynamics of the crust and mantle, *Phys. Earth Planet. Int.*, *163*, 69–82.
Moresi, L. N., and V. S. Solomatov (1998), Mantle convection with a brittle lithosphere: Thoughts on the global tectonic style of the Earth and Venus, *Geophys. J. Int.*, *133*, 669–682.
Morra, G., K. Regenauer-Lieb, and D. Giardini (2006), Curvature of oceanic arcs, *Geology*, *34*, 877–880.
Mueller, C., B. Bayer, A. Eckstaller, and H. Miller (2008), Mantle flow in the South Sandwich subduction environment from source-side shear wave splitting, *Geophys. Res. Lett.*, *35*, doi:10.1029/2007GL032411.
Nicolas, A., F. Boudier, and A. M. Boullier (1973), Mechanisms of flow in naturally and experimentally deformed peridotites, *Am. J. Sci.*, *273*, 853–876.
Nicolas, A., and N. I. Christensen (1987), Formation of anisotropy in upper mantle peridotites: A review, in *Composition, Structure and Dynamics of the Lithosphere-Asthenosphere System, Geodyn. Ser.*, vol. 16, edited by K. Fuchs and C. Froidevaux, pp. 111–123, AGU, Washington, D. C., doi:10.1029/GD016p0111.
Park, J., and V. Levin (2002), Geophysics: Seismic anisotropy: Tracing plate dynamics in the mantle, *Science*, *296*, 485–489.
Peyton, V., V. Levin, J. Park, M. Brandon, J. Lees, E. Gordeev, and A. Ozerov (2001), Mantle flow at a slab edge: Seismic anisotropy in the Kamchatka region, *Geophys. Res. Lett.*, *28*, 379–382.
Pidgeon, K., and M. K. Savage (1997), Frequency-dependent anisotropy in Wellington, New Zealand, *Geophys. Res. Lett.*, *24*, 3297–3300.
Ribe, N. M. (1992), On the relation between seismic anisotropy and finite strain, *J. Geophys. Res.*, *97*, 8737–8747.
Richardson, R. M., S. C. Solomon, and N. H. Sleep (1979), Tectonic stress in the plates, *Rev. Geophys.*, *17*, 981–1019.
Russo, R. M., and P. G. Silver (1994), Trench-parallel flow beneath the Nazca plate from seismic anisotropy, *Science*, *263*, 1105–1111.
Schellart, W. P., D. R. Stegman, R. J. Farrington, and L. N. Moresi (2011), Influence of lateral slab edge distance on plate velocity, trench velocity, and subduction partitioning, *J. Geophys. Res.*, *116*, doi:10.1029/2011JB008535.
Schulte-Pelkum, V., and D. K. Blackman (2003), A synthesis of seismic *P* and *S* anisotropy, *Geophys. J. Int.*, *154*, 166–178.
Smith, G. P., D. A. Wiens, K. M. Fisher, L. M. Dorman, S. C. Webb, and J. A. Hildebrand (2001), A complex pattern of mantle flow in the Lau backarc, *Science*, *292*, 713–716.
Song, T.-R. A., and H. Kawakatsu (2012), Subduction of oceanic asthenosphere: Evidence from sub-slab seismic anisotropy, *Geophys. Res. Lett.*, *39*, doi:10.1029/2012GL052639.
Stegman, D. R., J. C. Freeman, W. P. Schellart, L. Moresi, and D. May (2006), Influence of trench width on subduction hinge retreat rates in 3-D models of slab rollback, *Geochem. Geophys. Geosyst.*, *7*, 1–22, doi:10.1029/2005GC001056.
Syracuse, E. M., and G. A. Abers (2006), Global compilation of variations in slab depth beneath arc volcanoes and implications, *Geochem. Geophys. Geosyst.*, *7*, doi:10.1029/2005GC001045.
Tommasi, A. (1998), Forward modeling of the development of seismic anisotropy in the upper mantle, *Earth Planet. Sci. Lett.*, *160*, 1–13.
Vavrycuk, V. (2005), Inversion for anisotropy from non-double couple components of moment tensors, *J. Geophys. Res.*, *109*, doi:10.1029/2003JB002926.
Wang, D., M. Mookherjee, Y. Xu, and S. Karato (2006), The effect of water on the electrical conductivity of olivine, *Nature*, *443*, 977–980.
Watanabe, T., H. Kasami, and S. Ohshima (2007), Compressional and shear wave velocities of serpentinized peridotities up to 200 MPa, *Earth Planets Space*, *59*, 233–244.
Wenk, H.-R., and C. N. Tomé (1999), Modeling dynamic recrystallization of olivine aggregates in simple shear, *J. Geophys. Res.*, *104*, 25,513–25,527.
Wood, B. J., and A. Corgne (2007), Mineralogy of the earth—Trace elements and hydrogen in the Earth's transition zone and lower mantle, in Treatise of Geophysics, vol. *2*, edited by G. D. Price, pp. 63–89, 4, Elsevier, Oxford.
Zandt, G., and E. Humphreys (2008), Toroidal mantle flow through the western U.S. slab window, *Geology*, *36*, 295–298.
Zhang, S., and S.-I. Karato (1995), Lattice preferred orientation of olivine aggregates deformed in simple shear, *Nature*, *375*, 774–777.
Zhu, G., T. V. Gerya, D. A. Yuen, S. Honda, T. Yoshida, and J. A. D. Connolly (2009), Three-dimensional dynamics of hydrous thermal-chemical plumes in the oceanic subduction zones, *Geochem. Geophys. Geosyst.*, *10*, doi:10.1029/2009GC002625.